Direct experimental measurements of velocity gradient fields in turbulent flows via high-resolution frequency-based dual-plane stereo PIV (DSPIV)

John A. Mullin[(1)] and Werner J.A. Dahm[(2)]

Laboratory for Turbulence & Combustion (LTC), Department of Aerospace Engineering

The University of Michigan, Ann Arbor, MI 48109-2140, USA

[(1)]e-mail: jmullin@umich.edu

[(2)]e-mail: wdahm@umich.edu

ABSTRACT

A new frequency-based dual-plane stereo particle image velocimetry (DSPIV) technique is presented for highly-resolved measurements of the full nine-component time-varying velocity gradient tensor fields $?u_i/?x_j(\mathbf{x},t)$ at the quasi-universal intermediate and small scales of turbulent flows, and its application is demonstrated to determine effects of the outer-scale Reynolds number Re_δ and mean strain rate S on the local structure, statistics, similarity and scaling of shear flow turbulence. The method is based on two simultaneous independent stereo PIV measurements in two differentially-spaced light-sheet planes. The use of different laser frequencies in conjunction with filters to separate the scattered light onto the two stereo camera pairs allows use of solid metal oxide seed particles that permit measurements in nonreacting flows as well as exothermic reacting turbulent flows. Results from fully-resolved DSPIV measurements are demonstrated for the velocity gradient tensor components $?u_i/?x_j(\mathbf{x},t)$, the strain rate tensor components $\varepsilon_{ij}(\mathbf{x},t)$, the vorticity vector components $\omega_i(\mathbf{x},t)$, the enstrophy and enstrophy production rate $\omega_i\omega_i(\mathbf{x},t)$ and $\omega_i\varepsilon_{ij}\omega_j(\mathbf{x},t)$, and the kinetic energy dissipation rate $2\nu\varepsilon_{ij}\varepsilon_{ij}(\mathbf{x},t)$ in a turbulent shear flow at outer-scale Reynolds numbers Re_δ = 6,000 and 30,000 at two different values of the local mean shear. Measured fields and statistics are presented with normalizations by the local inner variables (ν, λ_ν) and by local outer variables (u_c, δ). Tests based on measured divergence values and isotropy indicate that rms errors in the on-diagonal $(i = j)$ and off-diagonal $(i ? j)$ components of the measured velocity gradients are respectively, 11.7% and 8.9% without any resort to explicit smoothing or filtering.

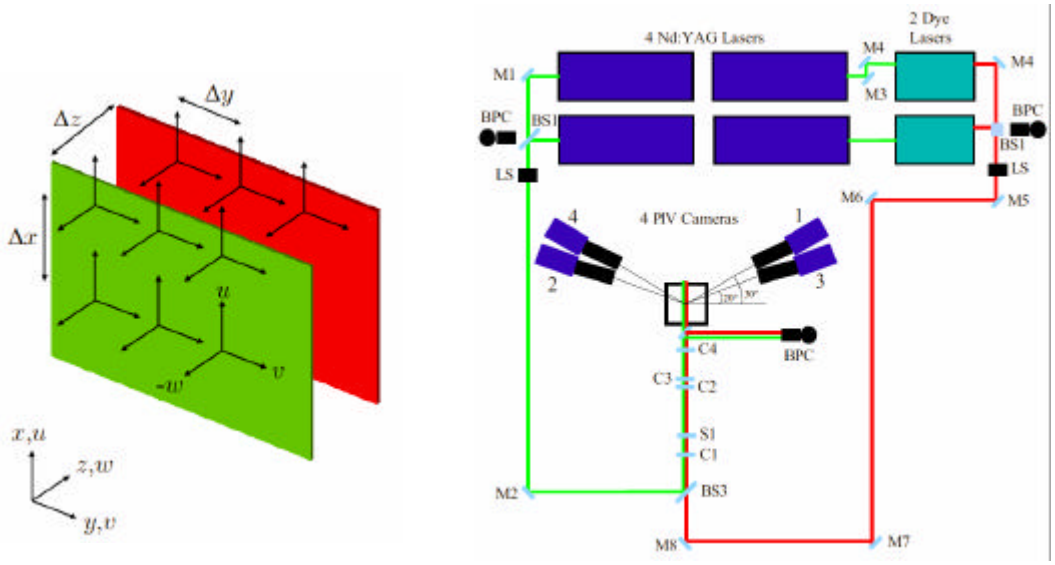

Fig. 1. Basic principle for frequency-based DSPIV, showing three-component stereo PIV measurements in two differentially-spaced light sheets (left), and present DSPIV system (right). Two Nd:YAG lasers provide the two green light sheets, and two others pump two dye lasers that provide the red light sheets.

1. INTRODUCTION

A significant amount of effort has been devoted in turbulence research toward developing models for the quasi-universal intermediate and small scales of both nonreacting and highly exothermic reacting turbulent flows. One approach to doing this is to base such models on the physical structure and temporal dynamics of key gradient fields at these scales. Key among these gradient fields are the strain rate tensor and vorticity vector fields, as well as the kinetic energy dissipation rate field, all of which can be obtained from the complete velocity gradient tensor field $?u_i/?x_j$ (**x**,*t*) However experimental measurement of all nine simultaneous components of the velocity gradients at the intermediate and small scales of turbulent flows is a significantly nontrivial matter. As a result, these gradient fields have to date been studied primarily by direct numerical simulations of homogeneous isotropic and sheared turbulence in periodic domains. While such simulations have provided important insights into the likely structure and dynamics of real shear flow turbulence, relatively little direct information has been available on the complete velocity gradient tensor fields in turbulent shear flows, where the combined effects of large-scale structure, inhomogeneities, and anisotropies inherent in such a flow can potentially lead to significant changes in the turbulence.

Experimental studies of velocity gradients in turbulent flows have used multiple hot-wire probes together with Taylor's hypothesis to simultaneously measure several components of the gradient tensor. These include probes with up to 20 hot-wires that measure all nine components of the velocity gradient tensor (*e.g.*, Tsinober *et al* 1992). Particle image velocimetry (PIV) subsequently allowed simultaneous nonintrusive measurement of two in-plane velocity components, here denoted $u(x,y)$ and $v(x,y)$. These provided four of the nine velocity gradient tensor components $?u_i/?x_j$, which in turn gave access to three of the six components of the strain rate tensor and a single vorticity component ω_z. Stereo PIV, dual-plane PIV, and scanning PIV allow additional measurement the out-of-plane velocity component $w(x,y)$ and thus provide the two further velocity gradient components $?w/?x$ and $?w/?y$. However two additional gradient components do not give access to any additional components of either the strain rate or the vorticity. Particle tracking velocimetry (PTV) provides three-component velocity fields throughout a three-dimensional volume, however the comparatively low spatial resolution imposed by the large particle separations needed to allow accurate particle tracking prevents velocity gradient measurements at the intermediate and small scales of turbulence. Resolution issues also prevent holographic particle image velocimetry (HPIV) from providing velocity gradient fields at the smallest scales in turbulent flows, though such measurements have provided important information at larger scales (*e.g.*, Zhang *et al* 1997, Meneveau & Katz 2000, van der Bos *et al* 2002). Fully-resolved indirect measurements via scalar imaging velocimetry (SIV) are based on three-dimensional laser-induced fluorescence imaging of a scalar field, and inversion of the conserved scalar transport equation from the measured scalar field data to obtain the underlying three-component velocity field. This has allowed the first noninvasive measurements of all nine simultaneous components of the velocity gradients at the intermediate and small scales of a turbulent flow (Dahm *et al* 1992, Su and Dahm 1996*a,b*). However such indirect measurements from measured scalar field data require additional smoothness and continuity constraints in the inversion to obtain the

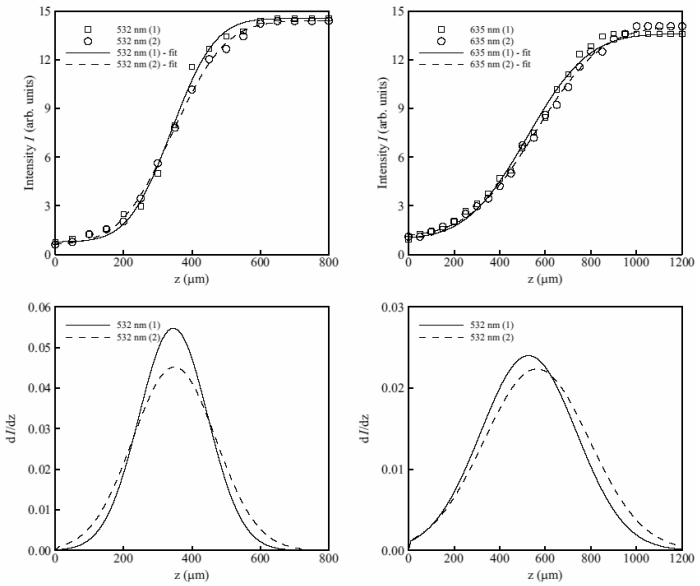

Fig. 2. Typical results for laser sheet profile measurements for the two green sheets (left) and the two red sheets (right), showing raw measured values (symbols) with error function fits (lines) at top, and derivative profiles at bottom giving local centroid position and thickness of each sheet.

velocity field data.
A polarization-based dual-plane stereo particle image velocimetry method was first reported by Kähler & Kompenhans (1999). That study used two stereo PIV systems to provide all three components of velocity in two parallel light sheets, with orthogonal polarizations in the two light sheets used to separate the scattered light from particles in the two sheets onto two independent stereo camera pairs. This allowed all nine components of the velocity gradients to be determined from the measured velocities in the two light-sheet planes. Kähler *et al* (2002) used this to measure comparatively large-scale features of the flow in a turbulent boundary layer, and Hu *et al* (2001) used the same technique to investigate large-scale features of a lobed jet mixer. However neither of these studies attempted to resolve the velocity gradients on the quasi-universal intermediate and small scales of turbulent flows. Moreover, to maintain the orthogonal polarization in the Mie scattered light required the scattering particles to be spherical, and these studies thus used fine liquid droplets as the seed particles. This can be done in nonreacting turbulent flows, but in exothermic reacting flows such liquid droplets do not survive and the polarization-based method cannot be used.

The frequency-based DSPIV approach presented here allows the first direct fully-resolved noninvasive measurements of all nine components of the velocity gradient tensor field $?u_i/?x_j$ at the intermediate and small scales of turbulent flows. As indicated in Fig. 1, the technique is based on two independent stereo PIV measurements using two different laser frequencies in conjunction with filters to separate the light scattered from the seed particles onto the individual stereo camera pairs. This allows traditional solid metal oxide particles to be used as the seed, and thus permits frequency-based DSPIV measurements to be made in reacting as well as nonreacting flows. Moreover, the thickness and differential spacing of the two light sheets in the present study allows the resolution in such velocity gradient measurements to reach below the strain-limited inner (viscous) diffusion scale λ_v of the turbulent flow.

Here we describe this frequency-based DSPIV technique and present assessments of the accuracy of velocity gradient measurements achievable from it. We also demonstrate its application to measuring fully-resolved velocity gradient fields in turbulent shear flow at various outer-scale Reynolds numbers Re_δ. A more complete description of this DSPIV method can be found in Mullin & Dahm (2004*a*), and detailed validation tests and assessments of the accuracy of such measurements are given by Mullin & Dahm (2004*b*). Detailed results for the structure, statistics, similarity, and scaling of turbulence at the intermediate and small scales of a turbulent shear flow under various conditions are given by Mullin & Dahm (2004*c*). Additional details of the DSPIV method can also be found in Mullin (2004).

2. EXPERIMENTAL TECHNIQUE

The frequency-based DSPIV system in Fig. 1 consists of four Nd:YAG lasers, two pulsed dye lasers, and four CCD cameras coordinated by a single computer with a programmable timing unit. These provide two essentially independent stereo PIV systems that simultaneously provide measurements in two differentially-spaced (400 μm) data planes. Each

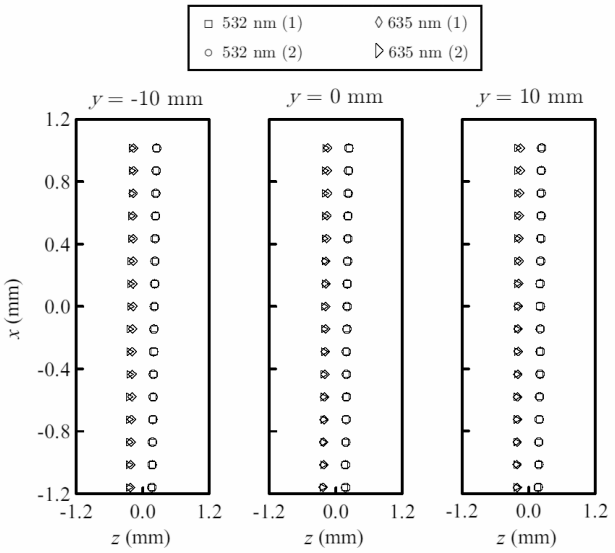

Fig. 3. Centroid positions of the four laser sheets determined from sheet profiles of the type in Fig. 2, showing measured results at the left edge (left), at the center (center), and at the right edge (right) of the field-of-view, verifying laser sheet coincidence, separation, and parallelism.

stereo camera pair operates with a coincident pair of 532 nm or 635 nm laser light sheets that illuminate the particles. Aluminum oxide seed particles with 0.5 μm diameter were used; these meet standard criteria to assure that the particles accurately follow the fluid motion. Each individual 5 particle image is a single-color, double-frame, single-exposure PIV image acquired at an angle to the light-sheet normal, thus allowing two cameras oriented in a stereo configuration to determine the two in-plane velocity components and the one out-of-plane velocity component over the measurement field-of-view.

2.1 *Dual Light-Sheet Pair Formation*

The two pairs of light sheets were formed using four frequency-doubled Nd:YAG lasers. Two of these were sequentially triggered to create the double pulses for the 532 nm sheets at 40 mJ per sheet. The other two were sequentially triggered at the same two instants to first produce 532 nm pulses at 400 mJ per pulse, which then pumped two pulsed dye lasers to provide the double pulses for the 635 nm sheets at 40 mJ per sheet. The time delay ?t between pulses was controlled by a programmable timing unit; the present ?t = 95 μs pulse separations were sufficient to freeze the fluid motion.

The 532 nm and 635 nm pulse pairs were combined using a long-pass beamsplitter that reflected > 95% of the 532 nm pulse and transmitted > 85 % of the 635 nm pulse. The pulse pairs then traveled through common sheet-forming optics to produce the differentially-spaced sheets. An f = 100 mm concave cylindrical lens and an f = 250 mm convex-symmetric lens transformed each beam into a sheet with a height of 20 mm. An f = 250 mm convex-symmetric lens and an f = 25 mm plano-convex lens formed a reverse 10:1 Galilean telescope that reduced the laser sheet widths, and two plano-convex lenses (f = 60 mm and f = 80 mm) separated by 160 mm were used to produce the waist in the test section. The optics were arranged on a single optical rail to provide a common optical axis, and each optic was mounted on a micrometer stage to allow individual adjustments along and transverse to the optical axis. Due to the differing frequencies of the light sheets, their respective waists fell at slightly different locations. The diameters of the 635 nm laser beams were thus increased to match the waists of the 532 nm and 635 nm sheets.

2.2 *Light-Sheet Pair Coincidence and Parallelism*

The thickness, spacing, and parallelism of the two resulting pairs of differentially-spaced light sheets were measured to assure the accuracy and resolution of the resulting DSPIV measurements. The thicknesses were measured in the center of the field-of-view by traversing a knife edge across each sheet and collecting the transmitted light onto a photodiode detector. To quantify each sheet thickness, as shown in Fig. 2 an error function was fitted using a nonlinear least-squares match to the measured profile, and then differentiated to obtain a sheet-normal gaussian intensity profile. The three lowest-order moments computed from this Gaussian profile allowed the centerline position and the local $1/e^2$ thickness of each laser sheet to be determined. This light sheet characterization procedure was repeated at the right and left edges of the field-of-view to verify that the thickness of the four respective light sheets did not vary significantly over the field-of-view.

Velocity Component	$(u_i)_{rms}$	Single		Coincident	
		$(\Delta u_i)_{rms}$ (m/s)	$\frac{(\Delta u_i)_{rms}}{(u_i)_{rms}}$	$(\Delta u_i)_{rms}$ (m/s)	$\frac{(\Delta u_i)_{rms}}{(u_i)_{rms}}$
u	0.24	0.011	4.6%	0.021	8.8%
v	0.20	0.013	6.5%	0.017	8.5%
w	0.21	0.022	10.5%	0.034	16.2%

Fig. 5. Rms errors in velocity component differences Δu_i from single-plane imaging tests and from coincident-plane imaging test of the type in Fig. 4. Note that results from coincident-plane imaging tests indicate relative errors of 8-9% in the in-plane velocity components, and 16% in the out-of-plane component.

Coincidence of each of the 532 nm and 635 nm light sheet pairs is required to minimize loss of particle pairs due to sheet misalignment, and the separation between the 532 nm and 635 nm light sheets affects the *z*-derivative resolution of the velocity gradients. The procedure for aligning the respective laser sheet pairs initially aligned the 532 nm and 635 nm beam pairs to be coincident over the length of the optical path. The coincidence was verified optically using CCD cameras and a centroid-finding image processing routine based on the beam spot intensities that allowed alignment of the centroids to within ±25 μm. The respective optical paths were aligned individually, without the sheet forming optics, and the beams were then formed into light sheets by inserting the spherical and cylindrical lenses. Separation of the two measurement planes began with the two light sheet pairs initially coincident. The 635 nm sheets were then moved by rotation of a mirror to provide the 400 µm *z*-separation between the 532 nm and 635 nm planes.

A small fraction (< 5%) of the energy in each of the two 532 nm and the two 635 nm light sheets was picked off prior to the test section to image the sheet cross-section on the BPC camera. Laser sheet intensity profiles were obtained by averaging every 16 rows in these images, with gaussian fits providing the local sheet-center location for each of the four laser sheets. Figure 3 shows typical results for the respective laser sheet centroids along the vertical direction for all four laser sheets. These verified that each sheet pair was essentially coincident, and that the spacing between the 532 nm

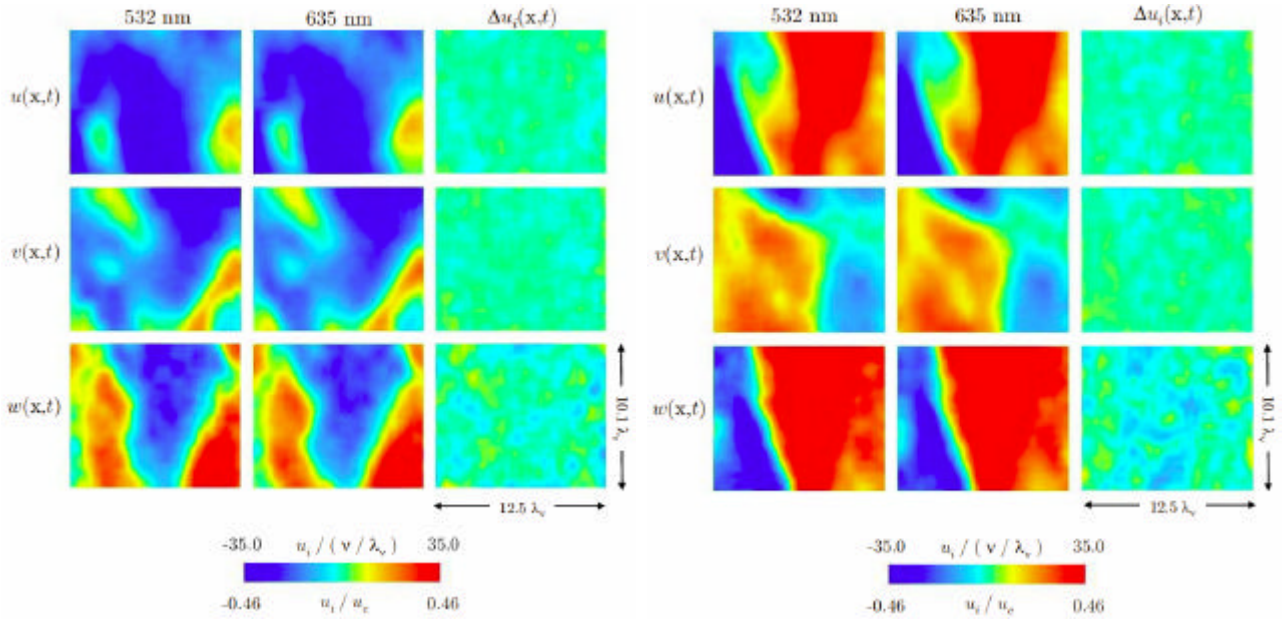

Fig. 4. Two typical instantaneous velocity component fields $u_i(\mathbf{x},t)$ from coincident-plane imaging tests, showing independently-measured fields from 532 nm (left) and 635 nm (middle) stereo camera pairs, and corresponding difference fields $\Delta u_i(\mathbf{x},t)$ (right) on same color scale.

and 635 nm planes was essentially uniform along the vertical direction. Coincidence and parallelism of the four light sheets over the entire field-of-view of the measurement was verified as shown in Fig. 3 by repeating this procedure at the left (y = –10 mm), center (y = 0 mm), and right (y = +10 mm) edges of the field-of-view. Results verified that the 532 nm and 635 nm sheets were coincident and remained parallel to within slightly less than 1-degree.

2.3. *Asymmetric DSPIV Imaging Arrangement*

Scattered light from the aluminium oxide seed particles was recorded on four 1280 × 1024-pixel 12-bit interline-transfer CCD cameras, which provided sufficient spatial dynamic range and signal dynamic range in the particle images. The field-of-view was 15.5 mm × 12.5 mm, giving a magnification of 0.55 based on the physical size of the CCD chip (8.6 mm × 6.8 mm). Each camera was equipped with a Sigma 70-300 f/4-5.6 APO macro lens that allowed up to 1:1 imaging at a minimum focal length of 40.1 cm to achieve the desired field-of-view. The 532 nm camera pair was equipped with narrow-band filters centered at 532 ± 5 nm to block the 635 nm light, and the 635 nm cameras were equipped with OG570 Schott glass filters that effectively blocked the 532 nm light.

The four cameras were arranged in an asymmetric angular-displacement configuration. The small field-of-view of the measurements, coupled with the long focal length of the camera lens, dictated that a large f # aperture to provide sufficiently-focused particle images over the measurement field-of-view. Each pair of stereo cameras was orientated so that the total included angle between the optical axes of each camera pair was 50 degrees. A more traditional symmetric forward/backward camera configuration was not used due to the decreased signal-to-noise level in backward scattering mode and the limited energy available in the laser sheets. In the present forward/forward camera configuration, one camera from each pair was arranged with a viewing angle of 20-degrees and the other at 30-degrees. The results of Coudert *et al* (2000) for asymmetric camera configurations indicate that the present 50-degree included angle and 10-degree asymmetry angle should give the error ratio to be about 1 to 2. This is similar to the values obtained for many symmetric SPIV arrangements, indicating that effects of the asymmetry in the camera arrangement are essentially negligible for the present small asymmetry angle.

2.4. *Particle Image Processing*

Particle images were processed by a cross-correlation method with a standard FFT-based algorithm, using an adaptive multi-pass approach with 32 × 32 pixel interrogation boxes on the first pass and then refining the correlation peak search on a second 32 × 32 pixel interrogation pass. This produced a final in-plane spatial resolution of 400 μm based on the physical pixel size of the CCD array, the magnification, and the interrogation box size. No overlap was used in the final vector field, allowing the in-plane and out-of-plane spatial resolution to be matched. Resulting velocity fields were further processed to replace spurious vectors (<10% of total vectors) by interpolation with a 3 × 3 median filter, and subsequently processed with a 3 × 3 median smoothing filter to reduce high-frequency noise.

Velocity gradients were computed using linear central-differencing in the x- and y-directions and one-sided differencing in the z-direction of the measured velocity fields to obtain all nine components of $?u_i/?x_j$. The gradient components were calculated on a standard 3 × 3 template that incorporates two independent coordinate frames, oriented at 45-degrees relative to each other, to provide two separate estimates of the gradient components that were averaged to obtain the final values; this makes use of all eight surrounding points for the in-plane gradient components and all five surrounding points for the out-of-plane gradient components.

2.5. *Overall Measurement Resolution*

The spatial resolution of these DSPIV measurements is determined by (*i*) the laser sheet thickness and separation, (*ii*) the PIV correlation window size, (*iii*) the typical bad-vector replacement region size, and (*iv*) the PIV smoothing filter scale. The laser sheet thicknesses were measured as described above as $\lambda_1 \sim 400$ μm for the 532 nm sheets and $\lambda_1 \sim 800$ μm for the 635 nm sheets. The 32 × 32 pixel PIV correlation window, together with the pixel size and magnification ratio, effectively filtered the velocity field at a scale $\lambda_2 \sim 400$ μm. Based on the spacing of the vectors, the bad-vector replacement scale was $\lambda_3 \sim 800$ μm, and the explicit filtering in the final processing stage was done at a scale $\lambda_4 \sim 800$ μm. The resulting gradient fields were thus resolved to a scale of $\lambda_{net} = (\lambda_1^2 + \lambda_2^2 + \lambda_3^2 + \lambda_4^2)^{1/2} \sim 1400$ μm.

3. ASSESSMENTS OF DSPIV ACCURACY

Assessments of the accuracy of velocity gradient measurements with this DSPIV approach can be obtained from tests based on single-plane and coincident-plane imaging. In single-plane tests, both stereo camera pairs in the DSPIV system are arranged to image the same particle field in the same double-pulsed light sheet. The velocity fields from the two camera pairs should then be identical, and differences in the two independently-measured fields allow quantitative determination of the accuracy with which velocity gradients can be measured. Assessment of the additional errors due to light sheet positioning inaccuracies and separate formation of green and red light sheet pairs can be obtained from tests based on coincident-plane imaging, in which the velocity fields obtained from the two independent stereo camera pairs are compared when the 532 nm and 635 nm light sheets are arranged to be as nearly coincident as possible, namely with $\Delta z \approx 0$.

Such imaging assessments were made on the centerline in the self-similar far field of an axisymmetric coflowing turbulent jet. Details of the flow facility are given by Mullin (2004). Air seeded with 0.5 μm aluminum oxide particles issued from a 1.0 m long tube with 2.2 mm inner diameter at nominal exit velocity U_o = 12.7 m/s into a uniformly seeded coflowing air stream in a 30 × 30 cm test section at coflow velocity U_1 = 0.25 m/s. Measurements were made 17 cm downstream of the nozzle exit, corresponding to $(x/\theta) = 2.1$ where θ is the invariant momentum radius of the flow. This (x/θ) value is within the jet-like scaling limit of the coflowing jet. The local mean centerline velocity u_c = 1.2 m/s and local flow width δ = 7.5 cm give the local outer-scale Reynolds number Re_δ = 6,000.

Figure 4 shows two typical examples of the instantaneous velocity vector fields $u_i(\mathbf{x},t)$ obtained independently from the 532 nm and 635 nm stereo camera pairs in the coincident-plane imaging tests, as well as the differences $\Delta u_i(\mathbf{x},t)$ between the two sets of respective fields shown in the same quantitative color scale. It is apparent that the differences Δu_i between the two independent measurements are far smaller than the measured velocity component values themselves. Figure 5 summarizes typical results from both single-plane imaging assessments in this flow configuration, giving resulting rms values of the velocity components u_i and the differences Δu_i in the results from the two camera pairs. In single-plane tests the relative errors in the velocity differences are seen to be no more than 6% for the in-plane components and 10% for the out-of-plane components. It is apparent that the *w*-component differences are typically larger than the *u*- and *v*-component differences, due to the inherently larger errors in measuring the out-of-plane velocity component with stereo PIV systems. In coincident-plane tests the resulting relative errors in the velocity differences found to be approximately 8-9% for the in-plane components and 16% for the out-of-plane components.

Additional assessments of the accuracy of these DSPIV measurements of velocity gradients at the intermediate and small scales of turbulent shear flows can be based on isotropy tests and on divergence values obtained from separated-plane imaging tests. Results from such tests are presented in the following section.

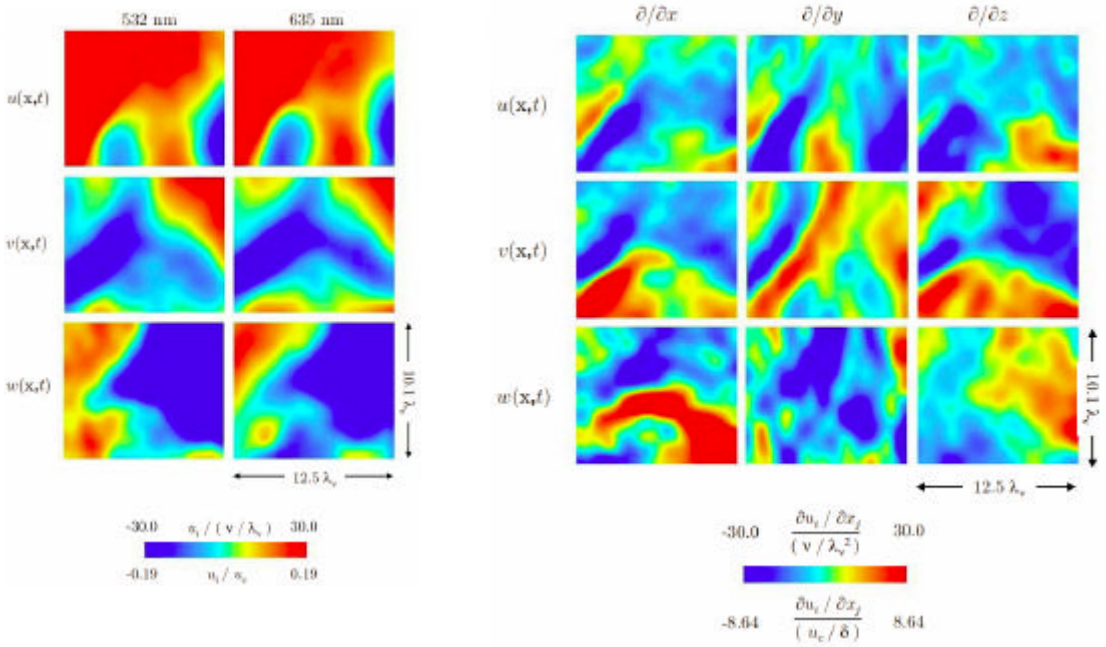

Fig. 7. Typical results from fully-resolved DSPIV measurements at radial location of maximum shear in a turbulent shear flow at Re_δ = 6,000, showing instantaneous velocity components $u_i(\mathbf{x},t)$ (left) in both imaging planes and corresponding nine-component velocity gradient tensor components $\partial u_i/\partial x_j(\mathbf{x},t)$ (right).

on the centerline of a turbulent shear flow at Re_δ = 6,000. Interplane separation is $\Delta z/\lambda_v$ = 0.32.

4. DEMONSTRATION OF DSPIV MEASUREMENTS

Further assessments of the accuracy of DSPIV velocity gradient measurements that take into account all nine simultaneously measured components of $?u_i/?x_j$ are possible from separated-plane imaging tests. Such assessments have been made in the same turbulent shear flow under identical conditions described above, but with the two stereo camera pairs now imaging individual 532 nm and 635 nm light sheets arranged with differential separation $\Delta z \approx 400$ μm matching the in-plane separation between adjacent vectors.

4.1 *Measured Velocity Gradient Fields*

Figures 6 and 7 give two typical examples of all three simultaneously-measured instantaneous velocity component fields $u_i(\mathbf{x},t)$ in two differentially-spaced 532 nm and 635 nm light sheet planes. The dimensions of each plane are indicated in terms of the local inner (viscous) length scale λ_v of the turbulent shear flow. The color scale gives the velocity component values normalized by the local outer velocity scale u_e as well as by the local inner velocity scale (ν/λ_v), and the size of each plane is given in terms on the inner length scale λ_v. Small differences discernible between the $u_i(\mathbf{x},t)$ fields in the 532 nm and 635 nm planes due to the differential z-spacing produce the z-derivative components of the velocity gradient tensor fields $?u_i/?x_j$. These same figures also show all nine simultaneously-measured components of the instantaneous velocity gradient tensor field $?u_i/?x_j$. The dimensions of major structural features in each of these velocity gradient component planes are consistent with the local inner length scale λ_v of the flow.

Probability densities of the three on-diagonal ($i = j$) and six off-diagonal ($i ? j$) components of the velocity gradients are given in both linear and semi-logarithmic forms in Fig. 8. These are formed from over 1200 individual data planes of the type in Figs. 6 and 7, each containing all nine gradient components at 736 independent points on the 32×23 grid. The similarity in the three on-diagonal component pdfs, and in the six off-diagonal component pdfs, is consistent with the requirements of isotropy. The semi-logarithmic forms in the lower panels of Fig. 8 verify that this similarity holds even for rare large-gradient features represented by the tails of these pdfs, which have a frequency of occurrence nearly 10^4 times lower than the mean. This provides further partial validation of the velocity gradients obtained from these DPSIV measurements. Moreover, the differing relative widths between the pdfs for the on- and off-diagonal velocity gradient components is consistent with the $\sqrt{?}$ difference expected for perfectly isotropic turbulence in incompressible flows. The average value of the second moments, normalized on inner variables, for the on-diagonal components is 6.93 and for the off-diagonal components is 9.64. The resulting ratio is 1.39, and is within 1.6% of the $\sqrt{?}$ for perfectly isotropic turbulence.

4.2 *Quantitative Assessment of Divergence Errors*

A further test of the validity of such DSPIV velocity gradient measurements is based on the measured divergence errors, namely the extent to which the resulting data satisfy the zero divergence condition ∇·**? ? ?**demanded by incompressibility. The measured divergence errors provide one of the most fundamental tests for the accuracy of any measurement of the full velocity gradient tensor. Zhang *et al* (1997) report divergence errors from holographic PIV measurements of velocity gradients in a turbulent flow, and the results in their Figs. 9 and 10 show that computation of the divergence over increasingly larger volumes leads to reduced error values. At the original measurement resolution W ≈ 930 μm, their reported mean divergence error $(?u_i/?x_i)^2$ is 74% of the local $(?u/?x)^2 + (?u/?y)^2 + (?u/?z)^2$ value.

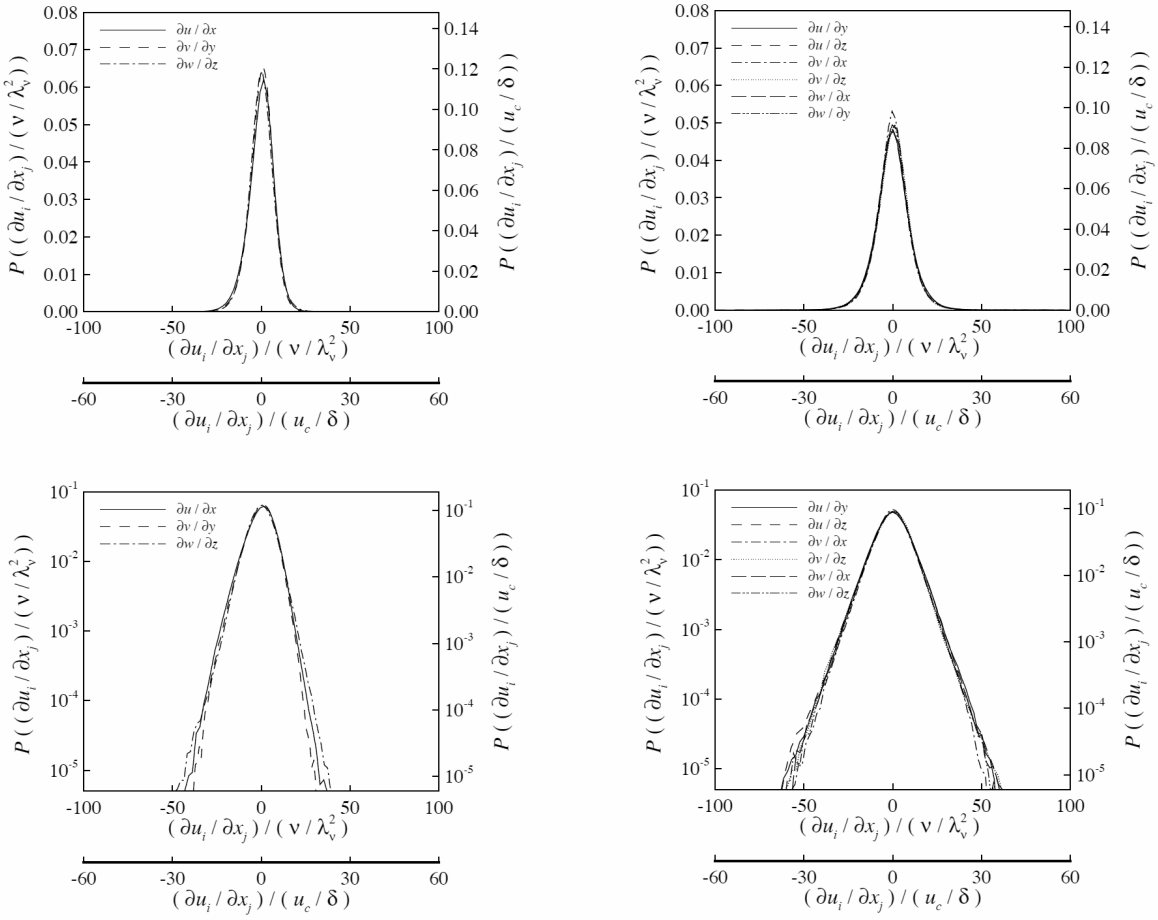

Fig. 8. Probability densities for on-diagonal (i = j) (left) and off-diagonal (i ? j) (right) components of velocity gradient tensor $?u_i/?x_j$ on centerline of a turbulent shear flow at Re_δ = 6,000, shown in linear (top) and semi-logarithmic (bottom) axes scales on local inner (ν, λ_ν) and outer (u_c,δ) variables.

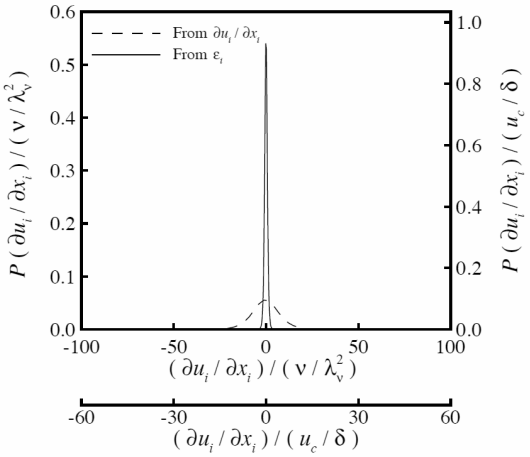

Fig. 9. Probability densities of divergence errors from fully-resolved DSPIV measurements in a turbulent shear flow at Re_δ = 6,000, shown on same scale as measured velocity gradient components in Fig. 8 for comparison. Rms divergence error from sum of principal strain rates is only 11.7% of rms on-diagonal gradient components values, and 8.9% of rms off-diagonal gradient components values.

There are several ways that $\nabla\cdot$**?** can be evaluated from the measured velocity gradient tensor components on the discrete measurement grid. All are equivalent in the continuous limit as the grid scale $\Delta \rightarrow 0$, but lead to differing discretization and truncation errors on any discrete grid (*i.e.*, when $\Delta > 0$). The smallest statistical error will result when equal use is made in the discrete derivative template of as many of the nine local velocity gradient components as possible. Templates that use the measured values at additional surrounding points on the grid are nonlocal and amount to filters applied to reduce the errors obtained from purely local derivative templates. Thus increasingly larger derivative templates can always be used to artificially decrease the resulting divergence values. Meaningful comparisons thus require $\nabla\cdot$**?** values obtained from the same-size template used to evaluate the velocity gradient components, as is done here in evaluating the divergence to assess the measured velocity gradient accuracies.

From these considerations, a naïve evaluation of $\nabla\cdot$**?** is obtained by summing the three on-diagonal components of the measured velocity gradients $?u_i/?x_j$. A better algorithm among purely local templates is to recognize that the divergence is the first invariant of the full velocity gradient tensor, and thus should be evaluated in a manner that makes use of all nine tensor components. This can be done by determining the three eigenvalues of the strain rate tensor from $?u_i/?x_j$, and then evaluating $\nabla\cdot$**?** as the sum of the three principal strain rates. Figure 9 gives probability densities of the resulting divergence errors for the present DSPIV measurements, from both the naïve evaluation based on the simple sum of the three on-diagonal components of $?u_i/?x_j$, as well as from the evaluation based on all nine components of $?u_i/?x_j$ via the sum of the three principal strain rates. It is apparent that there is a significant reduction in the divergence values when all nine local gradient components are used in the evaluation. If the nine components were independent, then a factor of $\sqrt{3} \approx 1.73$ reduction in the rms discretization error in $\nabla\cdot$**?** would be expected when using all nine components rather than just the three on-diagonal components. The rms values in Fig. 9 are 0.362 and 0.206 based on the three- and nine-component evaluations, respectively, giving a factor of 1.76 reduction in the rms discretization error by the use of all nine gradient components.

The resulting $\nabla\cdot$**?** values in Fig. 9, normalized by the inner and outer divergence scales (ν/λ_ν^2) and (u_c/δ), can be compared with correspondingly scaled values of the velocity gradient components in Fig. 8 to assess the accuracy of these gradient measurements. Note that the divergence errors are significantly smaller than the measured gradient component values themselves. The rms values of the divergence errors in Fig. 9 are 0.82 and 0.47 when scaled, respectively, on the inner and outer divergence scales, while the corresponding rms values of the on- and off-diagonal components of the measured velocity gradients $?u_i/?x_j$ in Fig. 8 are 6.4 and 9.0. Ratios of these values indicate typical errors of 11.7% in the on-diagonal gradient components and 8.9% in the off-diagonal components, consistent with the accuracy assessments based on the single-plane and the coincident-plane imaging tests in Fig.5.

4.2 *Strain Rate and Vorticity Fields, Enstrophy Fields, Enstrophy Production Rate Fields, and Kinetic Energy Dissipation Rate Fields*

Figure 10 shows a typical example of the instantaneous strain rate tensor and vorticity vector component fields, $\varepsilon_{ij}(\mathbf{x},t)$ and $\omega_i(\mathbf{x},t)$, obtained from such DSPIV measurements in a turbulent shear flow. From these gradient quantities, Fig. 11 shows the corresponding enstrophy field $\omega_i\omega_i(\mathbf{x},t)$, the enstrophy production rate field $\omega_i\varepsilon_{ij}\omega_j(\mathbf{x},t)$, and the kinetic energy dissipation rate field $2\nu\varepsilon_{ij}\varepsilon_{ij}(\mathbf{x},t)$ at three different conditions in a turbulent shear flow, corresponding to Re_δ = 6,000 and 30,000 and to radial locations of minimum and maximum local mean shear. Corresponding probability densities are presented in Fig. 12 with normalization by the local inner variables (ν, λ_ν) and by local outer variables (u_c, δ).

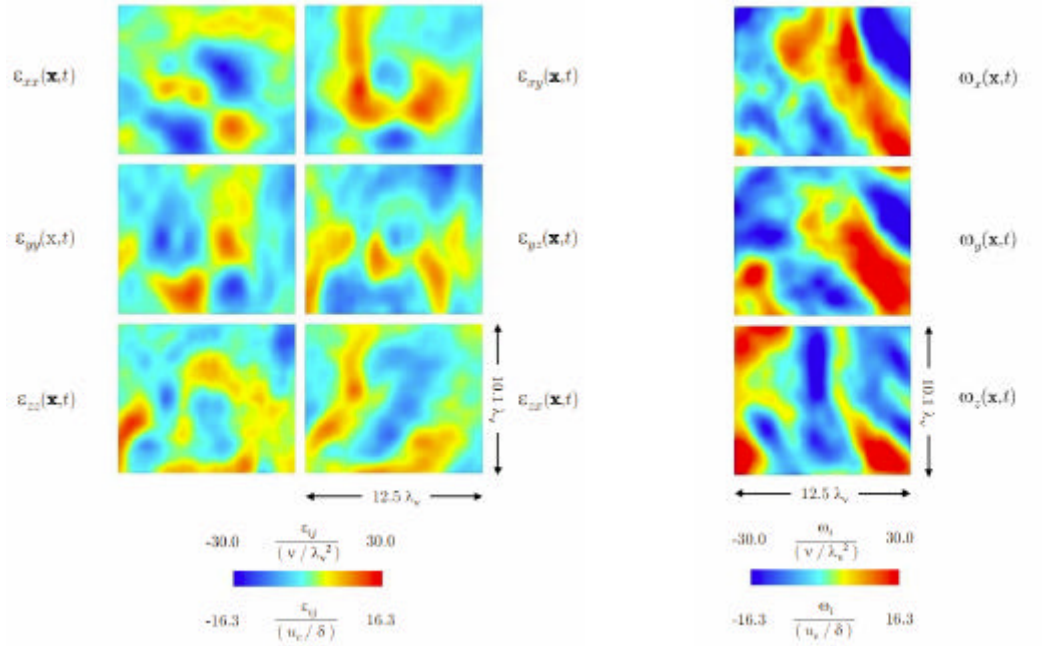

Fig. 10. Typical example of instantaneous six-component strain rate tensor field $\varepsilon_{ij}(\mathbf{x},t)$ (left) and three-component vorticity vector field $\omega_i(\mathbf{x},t)$ (right) from DSPIV measurements in a turbulent shear flow at Re_δ = 6,000. Field-of-view is shown normalized by local inner (viscous) length scale λ_ν, and color bars give values normalized on local inner (ν, λ_ν) and outer (u_c, δ) variables.

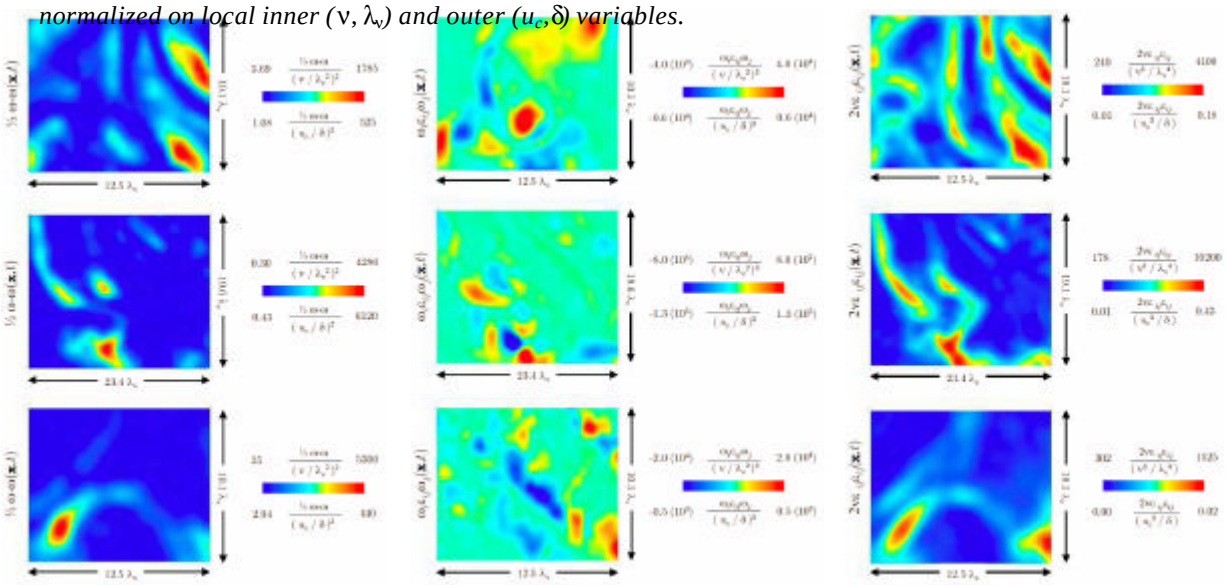

Fig. 11. Typical instantaneous DSPIV measurements of the enstrophy field $\omega_i\omega_i(\mathbf{x},t)$ (left column), the enstrophy production rate field $\omega_i\varepsilon_{ij}\omega_j(\mathbf{x},t)$ (middle column), and the kinetic energy dissipation rate field $2\nu\varepsilon_{ij}\varepsilon_{ij}(\mathbf{x},t)$ (right column) in a turbulent shear flow at Re_δ = 6,000 on centerline (top row), Re_δ = 6,000 at maximum shear (middle row), and Re_δ = 30,000 on centerline (bottom row).

Measurement results such as these can be used to study the structure, statistics, similarity, and scaling associated with key gradient fields at the quasi-universal intermediate and small scales of turbulent shear flows at conditions that are at

present significantly beyond the reach of direct numerical simulations. Such results are presented by Mullin & Dahm (2004*c*).

5. SUMMARY

Dual-plane stereo particle imaging velocimetry (DSPIV) using two different light-sheet frequencies allows direct nonintrusive fully-resolved measurements all nine simultaneous components of the velocity gradient tensor fields $?u_i/?x_j$ at the intermediate and small scales of turbulent flows. The use of two different laser frequencies, in conjunction with filters to separate the scattered light from seed particles onto the individual stereo camera pairs, allows traditional solid metal oxide particles to be used as the seed, and thereby permits such DSPIV measurements to be made in exothermic reacting flows as well as in nonreacting flows. Moreover, by properly arranging the components of such a DSPIV system, it is possible to resolve the quasi-universal intermediate and small scales of all velocity gradient components in turbulent flows, allowing direct experimental study of gradient fields such as the vorticity vector field, the strain rate tensor field, and the true kinetic energy dissipation rate field in turbulent flows. Results presented here demonstrate the key components of such a DSPIV system, the accuracy of the resulting measurements, and the ability to directly resolve the velocity gradients at the small scales of turbulent flows. Such DSPIV measurements provide the first direct

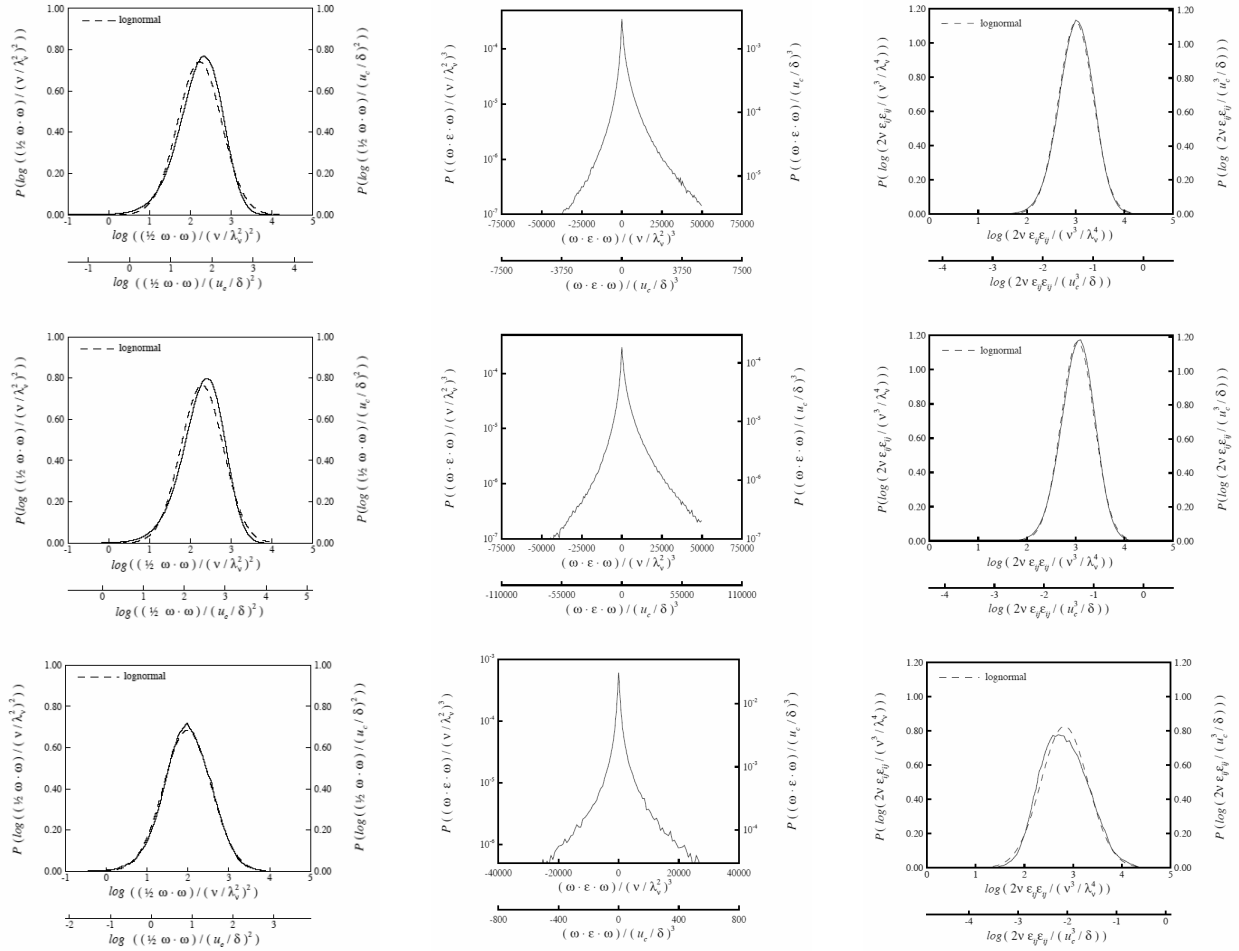

Fig. 12. Probability densities from DSPIV measurements of the enstrophy field $\omega_l \omega_l(\mathbf{x},t)$ (left column), the enstrophy production rate field $\omega_l \varepsilon_{ij} \omega_j(\mathbf{x},t)$ (middle column), and the kinetic energy dissipation rate field $2\nu\varepsilon_{ij}\varepsilon_{ij}(\mathbf{x},t)$ (right column) in a turbulent shear flow at Re_δ = 6,000 on centerline (top row), Re_δ = 6,000 at maximum shear (middle row), and Re_δ = 30,000 on centerline (bottom row).

nonintrusive experimental access to all nine simultaneous velocity gradient component fields at the intermediate and small scales of fully-developed turbulent shear flows under conditions that are, at present, beyond the reach of direct numerical simulation (DNS).

Acknowledgements

This work was supported by the NASA Glenn Research Center and Marshall Space Flight Center under NASA URETI Award No. NCC-3989, by NASA Award No. NGT3-52377, and by AFOSR Contract No. F49620-98-1-0003. The assistance of Mr. Zac Nagel from the Laboratory for Turbulence & Combustion (LTC) in the experiments, and of Dr. Callum Gray of LaVision GmbH with camera and software matters, is gratefully acknowledged. Dr. Cam Carter and Dr. Jeff Donbar of AFRL provided the dye lasers. Discussions with Prof. Nao Ninomiya from Utsunomiya University during two visits to LTC are also acknowledged.

REFERENCES

van der Bos, F., Tao, B., Meneveau, C. and Katz, J. (2002) Effects of small-scale turbulent motions on the filtered velocity gradient tensor as deduced from holographic particle image velocimetry measurements. *Phys. Fluids*, **14**, 2456-2474.

Coudert, S., Westerweel, J. and Fournel, T. (2000) Comparison between asymmetric and symmetric stereoscopic DPIV system. *Proc. 10th Int'l. Symp. on Appl.of Laser Tech. to Fluid Mech*., Lisbon, Portugal.

Dahm, W.J.A., Su, L.K. and Southerland, K.B. (1992) A scalar imaging velocimetry technique for fully resolved four-dimensional vector velocity field measurements in turbulent flows. *Phys. Fluids* **A4**, 2191-2206.

Hu, H., Saga, T., Kobayashi, T., Taniguchi, N. and Yasuki, M. (2001) Dual-plane stereoscopic particle image velocimetry: System set-up and its application on a lobed jet mixing flow. *Expts. Fluids* **31**, 277-293.

Kähler, C.J. and Kompenhans, J. (1999) Multiple plane stereo PIV: Technical realization and fluid mechanical significance. *Proc. 3rd International Workshop on PIV*, Santa Barbara, U.S.A.

Kähler, C.J., Stanislas, M. and Kompenhans, J. (2002) Spatio-temporal flow structure investigation of near-wall turbulence by means of multiplane stereo particle image velocimetry. *Proc. 11th Int'l. Symp. on Appl .of Laser Tech. to Fluid Mech*., Lisbon, Portugal.

Meneveau, C. and Katz, J. (2000) Scale-invariance and turbulence models for large-eddy simulation. *Annu. Rev. Fluid Mech.* **32**, 1-32.

Mullin, J.A. (2004) A study of velocity gradient fields at the intermediate and small scales of turbulent shear flows via dual-plane stereo particle image velocimetry. *Ph.D. Dissertation*, The University of Michigan, Ann Arbor, Michigan; also available for download as LTC Report No. 044475-3 at http://www.engin.umich/edu/dept/aero/ltc.

Mullin, J.A. and Dahm, W.J.A. (2004*a*) Dual-plane stereo particle image velocimetry (DSPIV) for measuring velocity gradient fields at intermediate and small scales of turbulent flows. *Expts. Fluids* (submitted); available for download as LTC Report No. 044475-4 at http://www.engin.umich/edu/dept/aero/ltc.

Mullin, J.A. and Dahm, W.J.A. (2004*b*) Dual-plane stereo particle image velocimetry measurements of velocity gradient tensor fields in turbulent shear flow. Part 1: Accuracy assessments. *Phys. Fluids* (submitted); available for download as LTC Report No. 044475-5 at http://www.engin.umich/edu/dept/aero/ltc.

Mullin, J.A. and Dahm, W.J.A. (2004*c*) Dual-plane stereo particle image velocimetry measurements of velocity gradient tensor fields in turbulent shear flow. Part 2: Experimental results. *Phys. Fluids* (submitted); available for download as LTC Report No. 044475-6 at http://www.engin.umich/edu/dept/aero/ltc.

Su, L.K. and Dahm, W.J.A. (1996*a*) Scalar imaging velocimetry measurements of the velocity gradient tensor field in turbulent flows. Part I. Assessment of errors. *Phys. Fluids* **8**, 1869-1882.

Su, L.K. and Dahm, W.J.A. (1996*b*) Scalar imaging velocimetry measurements of the velocity gradient tensor field in turbulent flows. Part II. Experimental results. *Phys. Fluids* **8**, 1883-1906.

Tsinober, A., Kit, E. and Dracos, R. (1992) Experimental investigation of the field of velocity gradients in turbulent flows. *J. Fluid Mech*., **242**, 169-192.

J. Zhang, J., Tao, B. and Katz, J. (1997) Turbulent flow measurement in a square duct with hybrid holographic PIV. *Expts. Fluids*. **23**, 373-381.